

Resolving the pathway to electronic liquid crystal phases in $\text{La}_{0.33}\text{Ca}_{0.67}\text{MnO}_3$

J. Tao^{1,*}, K. Sun², W. G. Yin¹, and Y. Zhu¹

¹Condensed Matter Physics & Materials Science Department, Brookhaven National
Laboratory, Upton, NY 11973

²Department of Physics, University of Michigan, Ann Arbor, MI 48109

Abstract

The characterization of the electronic liquid crystal phases in strongly correlated materials is of great importance in understanding the materials' structure-property relationship. Here we report the direct observations using transmission electron microscopy to resolve the real space evolution of the electronic structures in $\text{La}_{0.33}\text{Ca}_{0.67}\text{MnO}_3$. Specifically, we found that the diffraction measurements at the macroscopic scale from charge and orbital ordered structure are corresponding to distinct microscopic phenomena at the nanoscale and associated with different physical property measurements. Based on symmetry classification of the electron liquid-crystal phases, we identified the smectic, nematic, isotropic phases through thermal process. In addition, our findings suggest that the smectic-nematic and nematic-isotropic phase transitions are driven by two different electron phase separation scenarios as the key mechanism.

In the study of strongly correlated materials, it has long been known that novel phenomena can emerge from the melting of various ordered states, such as the high temperature superconductivity and the melting of the Neel ordering. In the vicinity of such a melting transition, electron liquid crystal (LC) phases, e. g., smecticity and nematicity which share strong analogy to LC phases from the symmetry perspective [1,2], have been observed in a wide range of strongly correlated systems and are believed to be essential in understanding the exotic quantum properties of these materials, including cuprates [3-6], bilayer ruthenates [7,8], Fe-based superconductors [1,9,10], two-dimensional electron gas under high magnetic field [11] and fractional quantum Hall systems [12]. Although extensive efforts have been devoted to the study of electronic LC states, many important questions remain open. In particular, the microscopic mechanisms that drive electronic LC phase transitions have not been fully understood. Diffraction techniques have been widely used to record the scattering reflections that are corresponding to the electron LC phases [7,13]. However, it has been challenging to correlate the characterizations of the electron LC phases at the macroscopic scale using diffraction results to what happened at the microscopic scale without real space observations. Consequently it is hard to interpret the electron LC phase transitions and connect them with thermal dynamic properties.

In this Letter, we report the direct observations of smectic-nematic and nematic-isotropic phase transitions upon warming in $\text{La}_{0.33}\text{Ca}_{0.67}\text{MnO}_3$ using transmission electron microscopy (TEM). In addition to characterizing these quantum phases by measuring global properties, i. e. the width, wavenumber and intensity anisotropy of the corresponding reflections from diffraction patterns, we observed real space phenomena at

the nanoscale that are responsible for the global characterizations. In particular, we imaged the formation of dislocations in the electronic structure, electron phase separation of the unidirectional electronic structure (electron phase separation scenario I) and emergence of anisotropic nanoscale domains (electron phase separation scenario II) during the phase transitions. We found that the smectic-nematic transition is driven by the electron phase separation scenario I that is mediated by the proliferation of the dislocations, while the electron phase separation scenario II plays key role in the nematic-isotropic phase transition. Our observations strongly favor the recently proposed theory by Nie and coworkers [14] which links the commensurate-incommensurate transition to the smecticity-nematicity transition. Moreover, our findings enable a better unification between electronic structures and other properties such as the crystal lattice variation and the specific heat measurements.

Complex spin-charge-orbital-lattice coupling in $\text{La}_{1-x}\text{Ca}_x\text{MnO}_3$ grants the material a rich phase diagram with a few intriguing properties such as colossal magnetoresistance [15] and giant magnetocaloric effects [16]. $\text{La}_{0.33}\text{Ca}_{0.67}\text{MnO}_3$ is known to have a low-temperature electronic phase with its superstructure along the a -axis and three-times larger than the fundamental-lattice unit cell at high temperatures (space group $Pnma$, $a \sim c = \frac{\sqrt{2}}{2} b$) [17,18]. Although the nature of the electronic superstructure is still under debate, to be charge and orbital ordering or charge density wave [17-22], the strong coupling between the electronic structure and the crystal lattice in this material causes superlattice modulation of the crystal. Taking advantage of the characteristic superlattice reflections (SLRs) in electron diffraction, the superstructure can be imaged in real space with stripe-like contrast as the projection of the three-dimensional superstructure [23], as

demonstrated in the dark-field TEM images at $T = 98$ K in Fig. 1a. Note that there is no SLRs along the c^* direction in the diffraction pattern at low temperatures. In the symmetry classification, this unidirectional modulation or the stripe phase represents an electronic smectic state. Upon warming, this smectic state melts and the intensity of the diffuse scattering along the c^* direction in the diffraction pattern (Fig. 1a) starts to rise. The global properties of the stripe order were characterized by measuring the wavenumber and full width at half maximum (FWHM) of the SLRs along a^* direction as a function of temperature (Fig. 1b). In addition, we examined the anisotropy of the electronic structure by measuring the value of $(I_a - I_c)/(I_a + I_c)$, which serves as the nematic order parameter with I_a and I_c being the SLR intensities along a^* and c^* directions. All the measurements were normalized for better comparison. As shown in Fig. 1b, the nematic order parameter shows a sharp rise upon cooling around at 310K, indicating long-range nematic ordering below this temperature. This nematic order parameter also shows a strong correlation to the lattice constant of the crystal measurements of both the a -axis and c -axis, indicating that the nematic ordering indeed has a direct impact on the property of the material (see supplemental material for details in crystal synthesis and electron diffraction analysis methods. Fig. S1 provides the comparison of all the measurements with the lattice constants).

Although the electronic LC phases can be clearly identified using the macroscopic measurements from the electron diffraction results (Fig. 1b), the electronic phase transition temperatures are difficult to be precisely determined from those plots, especially for the smectic-nematic transition. It can be seen that the width (FWHM), wavenumber and anisotropy plots provide three different characteristic temperatures as

their values start to change upon warming, ranging from 200 K to 250 K. Firstly, we want to emphasize that T_a , measured from the anisotropy plot, cannot be related to the smectic-nematic phase transition because both the two phases have rotational symmetry breaking. Secondly, the width measurements start to increase at low temperatures and the increase rate becomes very noticeable at T_w about 208 K. However, due to the absence of any sharp feature in the width measurements, it is hard to identify an accurate transition temperature. A better demonstration of this point can be seen in the smooth plot of the correlation length measurements as a function of temperature, which was converted from the FWHM plot, in the supporting fig. A1. Finally, the wavenumber plot shows a transition temperature $T_q \sim 223$ K in a commensurate-incommensurate phase transition, which in principle is a different concept as the smectic-nematic phase transition and the correlation between the two transitions remains unknown, yet.

In order to understand the microscopic mechanisms that drive the electronic LC phase transitions in this material, we explore the real space phenomena using direct observations. As shown in Fig. 2a the well-ordered low-temperature stripes start wiggling at 123 K in the dark-field TEM images upon warming. At 160 K, at which the FWHM started to increase, one pair of dislocations was found in the image by breaking a stripe from middle, pointed by white arrows. Another pair of dislocations, pointed by the red arrows, was just formed with very short separation distance. At 200 K, the FWHM continuously increased, and in the real space more pairs of dislocations were generated as pointed by yellow arrows, while the “white-arrow” pair and the “red-arrow” pair remain in the area with increased separation. When the temperature is further increased to 220 K,

the material shows electron phase separation with ordered and disordered areas with dislocations behaving as the melting core in the disordered region.

The direct observations in Fig. 2a offer insights linking the microscopic phenomena to the smectic-nematic phase transition. Because the observed dislocations stay in one area with no long-distance migration, we believe that they are induced by local disorders. The appearance of the dislocations directly caused the reduction in the coherent length, which is reflecting in the FWHM measurements. However, the existence of dislocations does not ruin the long-range stripe phase until the phase separations occur. The threshold of real-space phase separation is a more accurate way to determine the smectic-nematic phase boundary. Based on this description, the transition temperature is at ~ 220 K, which coincides with the commensurate-incommensurate transition temperature measured by the wavenumber plot. Remarkably, this scenario shows strong analogy to the recent theoretical proposal of vestigial nematicity [14], which predicts that for a 3D system at finite temperature, a commensurate stripe phase is stable against weak disorder while an infinitesimal amount of disorder will destroy an incommensurate stripe phase and turning it into a nematic state, i. e., the vestigial nematicity. The key signature of vestigial nematicity includes the existence of short-range incommensurate stripe ordering and coincidence between the smectic-nematic and the loss of commensurability, both of which were observed in our experiments.

Moreover, the direct observations may reveal the nature of the superstructure modulation as follows. The formation of the dislocation pairs observed in Fig. 2a shows an interesting “cutting-in-the-middle” and “pulling-again-each-other” behavior of the stripe order, which is similar to cutting springs, suggesting strong elastic property in the

stripe order in $\text{La}_{0.33}\text{Ca}_{0.67}\text{MnO}_3$. Since the stripe-like contrast in the dark-field images results from the atomic displacement wave in the modulation^{4,2}, we propose a melting mechanism of the stripe order shown in Fig. 2b and 2c. Thinking of an orbital disorder for one Mn^{3+} ion in Fig. 2b due to the thermal process, the orbital disorder causes movement of the neighboring Mn^{4+}O_6 octahedron based on the Wigner-crystal model² of the modulation, forcing the d_{z^2} orbital changing direction in the Mn^{3+}O_6 octahedra on top and bottom to compromise the elastic energy via a chain reaction as described in Fig. 2b. Our observations imply that the charge and orbital ordering with the Jahn-Teller (JT) distortion dominates the intrinsic properties of the smectic order in $\text{La}_{0.33}\text{Ca}_{0.67}\text{MnO}_3$. This is also consistent with the reported DFT calculations that orbital ordering with JT distortion is energetically favored at commensurate dopings in manganites [24,25].

We further explore the behavior of the electronic LC phases after the electronic phase separation occurs in $\text{La}_{0.33}\text{Ca}_{0.67}\text{MnO}_3$ at $T \sim 220$ K upon warming. The stripe-like superstructure modulation becomes short-range while the nematic order exists globally in the material. The contrast of the localized modulation is much weaker in the dark-field images comparing to the well-ordered stripe phase and the scanning electron nanodiffraction (SEND) is a powerful technique in mapping the electronic modulation at the nanoscale in bulk materials [26]. The principle of the SEND is to map the intensity of the SLRs in the electron nanodiffraction that acquired at each pixel during the beam scanning in real space in order to visualize the distribution of inhomogeneous phases in the crystal. A series of SEND maps, each is $22 \times 22 \text{ nm}^2$ in size, from 220 K to 281 K is shown in Fig. 3a with the color scale on the right. Specifically the green/blue color is corresponding to the disorder phase, and areas in red and purple colors have the

superstructure modulation along the a -axis and c -axis, respectively. We note not only the shrinking of the ordered areas in red but also the emergence of the ordered areas in purple from the disorder area with increased temperature from Fig. 3a. Although the electronic phase separation starts at $T \sim 220$ K, there is no observable purple nanocluster in the SEND maps until the temperature is above 248 K, which is in good agreement with the temperature T_a identified in Fig 1b by measuring anisotropy. This is because the short-range stripe orders in red and purple regions are along perpendicular directions. The mismatch in orientation shall result in an energy penalty at the domain boundary, which would suppress the formation of a purple domain at low temperature. The purple domain will only arise at above certain threshold temperature to overcome this energy penalty. It also implies that the abrupt emergence of the purple nanoclusters at ~ 248 K should be responsible for the sharp peak in the specific heat measurements reported at temperature ~ 245 K for the temperature coincidence [27]. As the temperature continuously increases, the purple domains emerge with increasing number and have nearly comparable size and density as the red domains before both of them disappear at temperature above 310 K, which reduces the anisotropy and eventually results in the nematic-isotropic phase transition.

Based on the scheme discussed above, we provide a mean-field theory to understand the formation of the dislocation pairs at low temperatures and the purple domains at high temperatures as shown in Figs. 2d and 3b. We first construct a Ginzburg–Landau (GL) free energy which prefers unidirectional density-wave order. We assume that due to the lattice anisotropy, the ordering wave-vector is pinned to the a -axis for most areas. However, due to disorder effect, a local region, marked by the red box in

Figs. 2d and 3b, prefers stripe order along the perpendicular direction. By numerically minimizing the GL free energy, at low-temperature when the amplitude of the density wave is large, a pair of dislocations is observed (Fig. 2d). At high temperatures, as the amplitude of the density wave decreases and thus the energy penalty at the domain boundary reduces, a local domain with stripe oriented in the perpendicular direction can be formed (Fig. 3b).

It is also worthwhile to highlight that the phenomena observed in $\text{La}_{0.33}\text{Ca}_{0.67}\text{MnO}_3$ are similar to reported observations in other strongly correlated materials, especially cuprates. For instance, the nanoclusters with short-range ordering in the nematicity at $T = 280$ K (Fig. 1a and Fig. 3a) are strikingly similar to the local electronic structure observed in the nematic phase in $\text{Bi}_2\text{Sr}_2\text{CaCu}_2\text{O}_{8+\delta}$ [6]. Moreover, it must also be noted that for $\text{La}_{0.33}\text{Ca}_{0.67}\text{MnO}_3$ the crystalline symmetry breaks from cubic to orthorhombic at 1100 K [28], suggesting that certain degree of anisotropy between the a and c directions is expected due to the orthorhombicity itself instead of the electronic nematic ordering. The subtleties to distinguish lattice anisotropy from correlated electronic effects have been understood in the study of nematicity in de-twinned $\text{YBa}_2\text{Cu}_3\text{O}_{6+x}$ single crystals, which also has an orthorhombic lattice [4,29]. Similar as in $\text{YBa}_2\text{Cu}_3\text{O}_{6+x}$, here the rapid rise of anisotropy near 310K upon cooling strongly indicates that this anisotropy is electronically driven, while the variation of lattice constant in this temperature range is a result of the electronic structural intricacies. Despite the strong analogy, the nematic state observed here has some fundamental differences in comparison to cuprates. Firstly, manganites are three-dimensional materials while cuprates have a layered structure. Secondly, the nematic modulation in doped manganites

is insulating, where the corresponding state in cuprates is metallic/superconducting. Thirdly, in cuprates, there can be a quantum phase transition between the nematic and smectic phases, driven by quantum fluctuations, the phase transitions that we observed are classical driven by thermal fluctuations. These differences change the critical scaling at the phase transition, as well as the stability of the ordered state against disorder or thermal fluctuations. However, at the qualitative level, especially from the symmetry perspective, the behavior of the nematicity in manganites depicted in this letter shows high level of consistency with other systems and the electron nematicity theory from a symmetry perspective. Therefore, our investigation would shed new light on the study of other strongly correlated materials with similar electronic phases and phase transitions.

We thank Prof. Jian-Min Zuo, Dr. Huolin Xin and Prof. Huaixin Yang for discussion of the dark-field TEM images and Dr. Maria Teresa Fernandez-Diaz for help on her previous measurements of lattice constants. This research is sponsored by the US Department of Energy (DOE)/Basic Energy Sciences, Materials Sciences and Engineering Division under Contract DE-AC02-98CH10886. KS is supported in part by NSF under Grant No. ECCS-1307744 and the MCubed program at University of Michigan.

References

*jtao@bnl.gov

- [1]. S. A. Kivelson, E. Fradkin & V. J. Emery, *Nature* **393**, 550 (1998).
- [2]. E. Fradkin, S. A. Kivelson, M. J. Lawler, J. P. Eisenstein, A. P. Mackenzie, *Annual Review of Condensed Matter Physics* **1**, 153 (2010).
- [3]. Y. Ando, K. Segawa, S. Komiyama, and A. N. Lavrov, *Phys. Rev. Lett.* **88**, 137005 (2002).
- [4]. V. Hinkov *et al.*, *Science* **319**, 597 (2008).
- [5]. A. Mesaros *et al.*, *Science* **333**, 426 (2011).
- [6]. Y. Kohsaka *et al.*, *Science* **315**, 1380 (2007).
- [7]. R. A. Borzi *et al.*, *Science* **315**, 214 (2007).
- [8]. S. Raghu *et al.*, *Phys. Rev. B* **79**, 214402 (2009).
- [9]. T.-M. Chuang *et al.*, *Science* **327**, 181 (2010).
- [10]. C. Fang, H. Yao, W.-F. Tsai, J. Hu, and S. A. Kivelson, *Phys. Rev. B* **77**, 224509 (2008).
- [11]. E. Fradkin, S. A. Kivelson, E. Manousakis, and K. Nho, *Phys. Rev. Lett.* **84**, 1982 (2000).
- [12]. J. Xia, *et al.*, *Nature Physics* **7**, 845 (2011).
- [13]. J. Chang, *et al.*, *Nature Physics* **8**, 871 (2012).
- [14]. L. Nie, G. Tarjus, S. A. Kivelson, arXiv: 1311.5580
- [15]. P. Schiffer, A. P. Ramirez, W. Bao, and S.-W. Cheong, *Phys. Rev. Lett.* **75**, 3336 (1995).
- [16]. X. Moya *et al.*, *Nature Materials* **12**, 52 (2013).
- [17]. C. H. Chen, S.-W. Cheong, and H. Y. Hwang, *J. Appl. Phys.* **81**, 15 (1997).
- [18]. P. G. Radaelli, D. E. Cox, L. Capogna, S.-W. Cheong, M. Marezio, *Phys. Rev. B* **59**, 14440 (1999).

- [19]. J. C. Loudon *et al.*, *Phys. Rev. Lett.* **94**, 097202 (2005).
- [20]. W. Luo *et al.*, *Phys. Rev. Lett.* **99**, 036402 (2007).
- [21]. S. Cox, J. Singleton, R. D. McDonald, A. Migliori and P. B. Littlewood, *Nature Materials* **7**, 25 (2008).
- [22]. B. Fisher *et al.*, *Nature Materials* **9**, 688 (2010).
- [23]. J. Tao and J. M. Zuo, *Phys. Rev. B* **69**, 180404 (2004).
- [24]. W.-G. Yin, D. Volja, and W. Ku, *Phys. Rev. Lett.* **96**, 116405 (2006).
- [25]. D. Volja, W.-G. Yin, and W. Ku, *EPL* **89**, 27008 (2010).
- [26]. J. Tao *et al.*, *Phys. Rev. Lett.* **103**, 097202 (2009).
- [27]. M. T. Ferna'ndez-Di'az, J. L. Marti'nez, J. M. Alonso, E. Herrero, *Phys. Rev. B* **59**, 1277 (1999).
- [28]. J. He, R. Wang, J. Gui and C. Dong, *Phys. Stat. Sol. (b)* **229**, No. 3, 1145 (2002).
- [29]. Y. Ando, K. Segawa, S. Komiya and A. N. Lavrov, *Phys. Rev. Lett.* **88**, 137005 (2002).

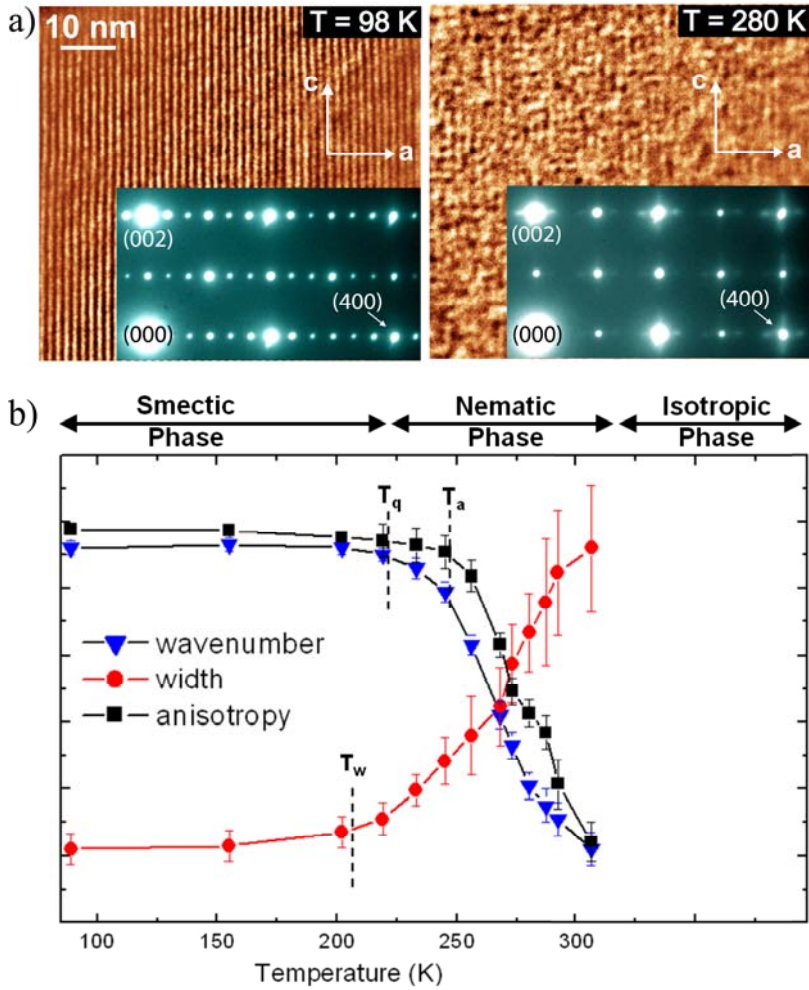


Figure. 1. (a) Dark-field TEM images obtained at $T = 98$ K showing a long-range stripe phase along the a -axis and at $T = 280$ K showing the short-range nanoclusters with the stripe-like contrast along the a -axis or the c -axis. The diffraction pattern of $[010]$ zone at each temperature is attached at the top-right corner. (b) The wavenumber, the FWHM measurements of the SLRs along a^* direction and the intensity anisotropy measured from the SLRs along a^* and c^* directions as a function of temperature. The electron LC phases were identified from these measurements.

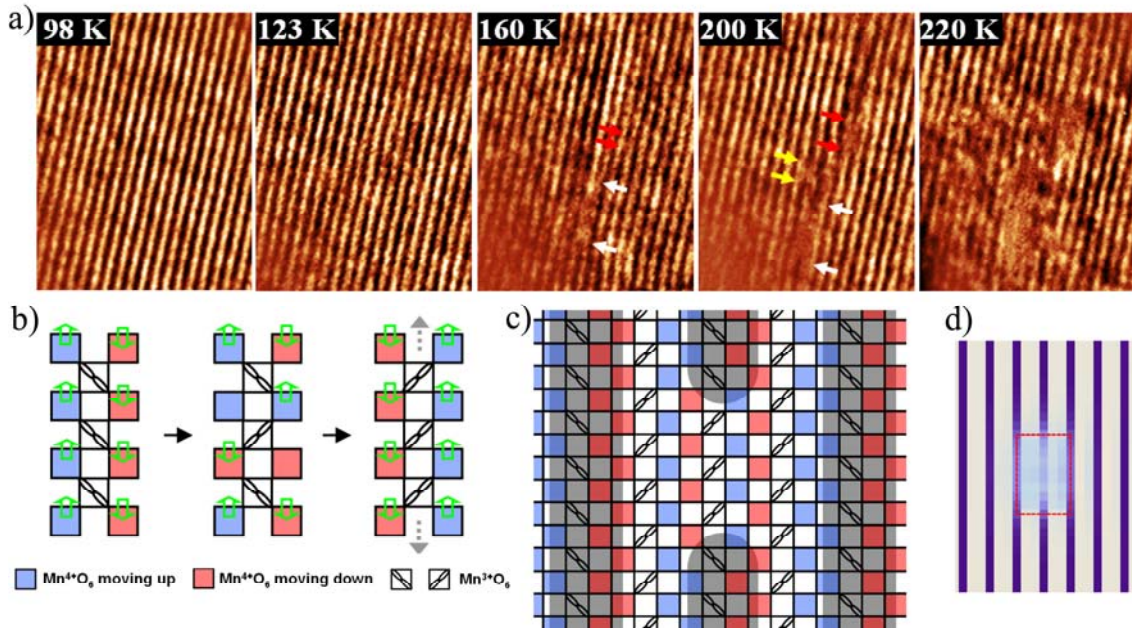


Figure 2. (a) A sequence of snapshots of dark-field TEM images recorded at different temperatures upon warming through the smectic-nematic phase transition in $\text{La}_{0.33}\text{Ca}_{0.67}\text{MnO}_3$. Each image is $\sim 30 \times 37$ nm in size. With the nearby defects as a marker (see supplemental Fig. S2), all the TEM images were well registered from the same area. Formation of pairs of dislocations is highlighted by the arrows. A model shown in (b) proposes a possible formation mechanism of a pair of dislocations in (c) that it starts with d_{z^2} orbital disorder in a Mn^{3+}O_6 octahedron and propagates along one stripe via elastic chain reaction. (d) Local electron density at low temperatures computed in the GL theory (see text for details).

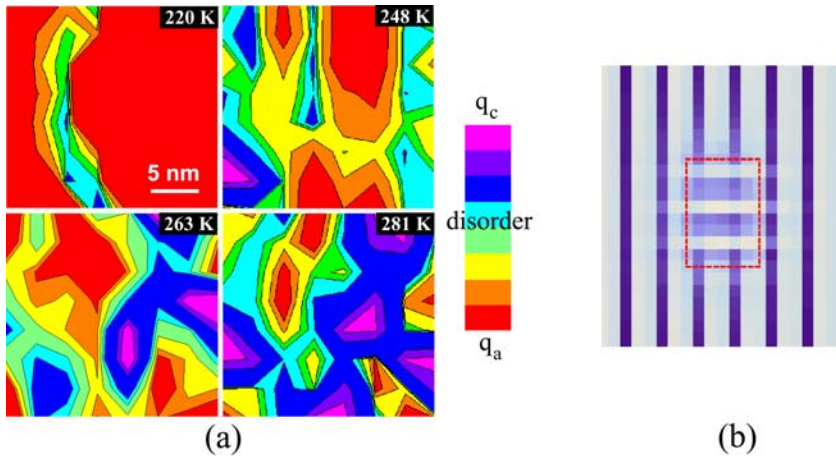


Figure. 3. (a) SEND maps obtained from $T = 220$ K to $T = 280$ K show two types of electron phase separation scenarios in a single-crystal domain. (b) Local electron density at high temperatures computed in the GL theory (see text for details).

Supplemental Material

The polycrystalline $\text{La}_{0.33}\text{Ca}_{0.67}\text{MnO}_3$ was synthesized using the method in ref. 15. The TEM results including the dark-field images and the electron diffraction patterns were obtained within single-crystal domains.

TEM dark-field images were obtained under the two-beam condition described in ref. 23. The images is formed by the interference of the satellite superlattice reflections and thus the stripe-like contrast in the images can be directly linked to the atomic displacement wave using the Wigner-crystal model shown in ref. 18.

The wavenumber, FWHM and the anisotropy of the superlattice reflections were analyzed using the same set of electron diffraction data obtained from a sample area about 200 nm in diameter. The FWHM measurements were deconvoluted from the effect due to the beam/illumination size. The transition temperatures of the lattice constant, the wavenumber, the FWHM and the anisotropy measurement were determined by the following method. Each plot was smoothed and the first derivative was calculated. The transition temperature was determined at the temperature when its first derivative reaches 15 % of the maximum value though the phase transitions upon warming.

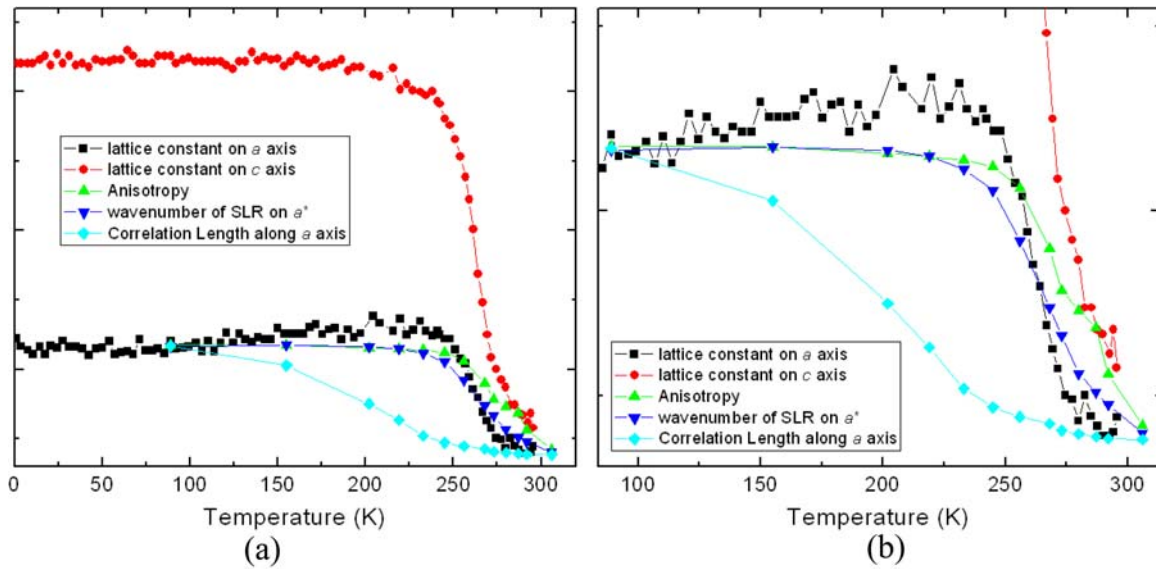


Figure S1. A comparison of all the measurements from the superlattice modulation and crystal lattice for $\text{La}_{0.33}\text{Ca}_{0.67}\text{MnO}_3$. The crystal lattice constants were excerpted from ref. 27. The correlation length is converted from the FWHM results. In order to have a better comparison particularly with the transition temperatures, the measurements of the anisotropy, the wavenumber and the correlation length are all normalized to the amplitude of the lattice constant on the a -axis. Part of plot (a) is enlarged as plot (b), showing details through the transition.

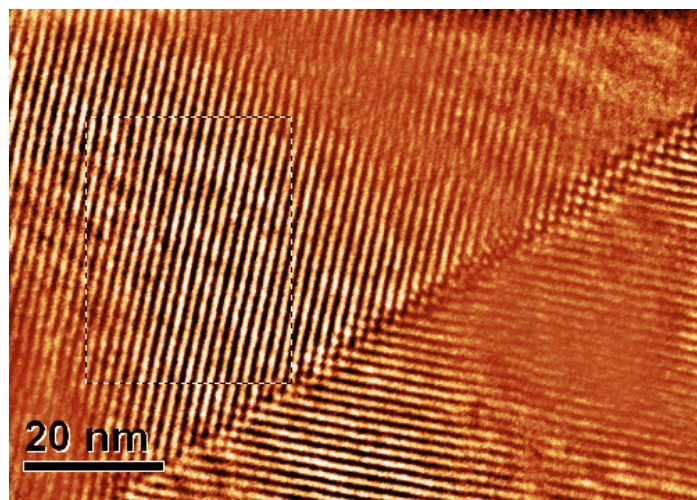


Figure S2. A dark-field TEM recorded from the low-temperature $\text{La}_{0.33}\text{Ca}_{0.67}\text{MnO}_3$ with crystalline domain boundary. The dash box shows the area where the TEM images in Fig. 2 were obtained.

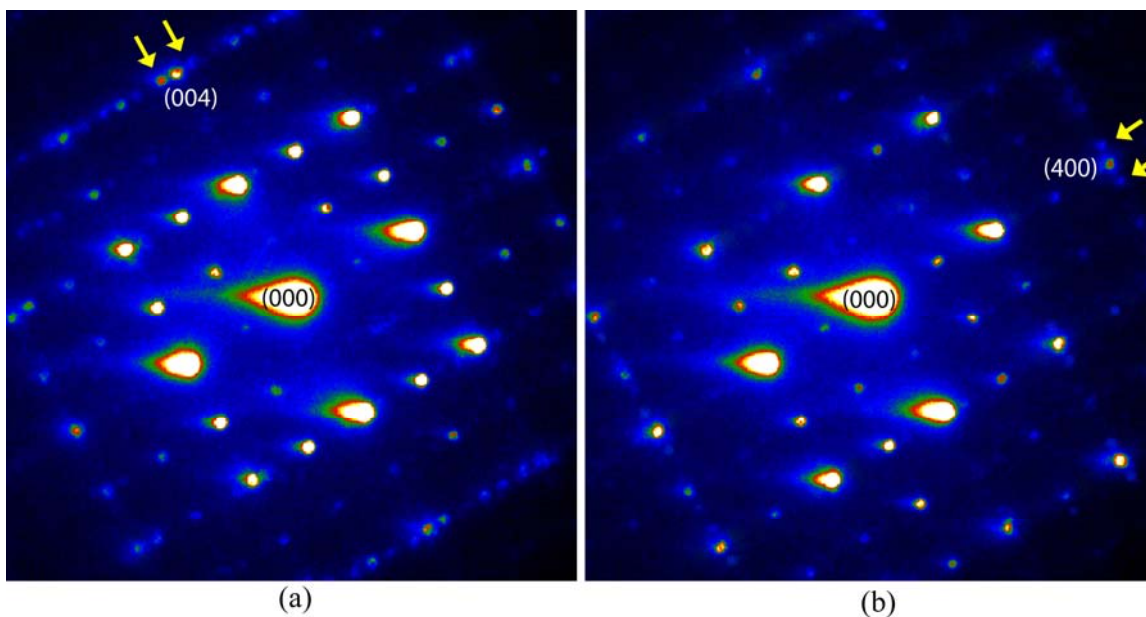


Figure S3. Two electron nanodiffraction (END) patterns obtained during the SEND mapping. Short-range ordering with SLRs along the a^* direction can be seen in (a), with typical ones around (004) reflection pointed by the yellow arrows. At somewhere else in the same single-crystal domain, short-range ordering with SLRs along the c^* direction were highlighted in (b) around (400) reflection by the yellow arrows.